Journal of Catalysis 278 (2011) 59–70

Contents lists available at ScienceDirect

Journal of Catalysis

journal homepage: www.elsevier.com/locate/jcat

Influence of particles alloying on the performances of Pt–Ru/CNT catalysts for selective hydrogenation

Jacques Teddy [a], Andrea Falqui [b], Anna Corrias [c], Daniela Carta [c], Pierre Lecante [d], Iann Gerber [e], Philippe Serp [a,*]

[a] Laboratoire de Chimie de Coordination, UPR CNRS 8241, Composante ENSIACET, Université de Toulouse UPS-INP-LCC, 4 allée Emile Monso, BP 44362, 31432 Toulouse Cedex 4, France
[b] Istituto Italiano di Tecnologia, Via Morego 30, 16163 Genova, Italy
[c] Dipartimento di Scienze Chimiche, Universita' di Cagliari, Cittadella Universitaria di Monserrato S.S. 554 Bivio per Sestu, 09042 Monserrato, Cagliari, Italy
[d] Centre d'Elaboration des Matériaux et d'Etudes Structurales du, CNRS, 29 rue Jeanne Marvig, BP 4347, 31055 Toulouse Cedex, France
[e] Université de Toulouse INSA, UPS, LPCNO, IRSAMC, 135 avenue de Rangueil, 31077 Toulouse, France

ARTICLE INFO

Article history:
Received 6 September 2010
Revised 19 November 2010
Accepted 20 November 2010
Available online 7 January 2011

Keywords:
Carbon nanotubes
Bimetallic catalysts
Selective hydrogenation
Platinum–ruthenium

ABSTRACT

The influence of PtRu bimetallic particle size and composition on cinnamaldehyde selective hydrogenation has been investigated for the first time using well-defined catalysts based on carbon nanotubes support. Very high selectivity towards cinnamyl alcohol together with high activity have been obtained provided a high temperature treatment of the catalyst is performed. HRTEM, WAXS and EXAFS analyses permit us to conclude that the remarkable influence of this high temperature treatment on both activity and selectivity arises from different phenomena. First, a particle size and a structural effect have been evidence that permits to increase the selectivity. WAXS and EXAFS point the formation of alloyed PtRu nanoparticles. Second, the heat treatment allows the removal of oxygenated groups from CNT surface. This may increase the cinnamaldehyde adsorption capacity and decrease the activation barrier for diffusion of substrate and product on the CNT surface, thus contributing to an increase in the activity.

1. Introduction

If, during most of the 20th century, the main motivation in catalysis was productivity, at the beginning of the 21st century the concepts of sustainable growth and *Green Chemistry* are at the center of the chemical activity and the research of a high selectivity is the driving force for the conception of all new catalytic processes. Thus, today a catalyst must associate three characteristics: high activity and selectivity as well as stability (separation, recovery, recycling). From now on, the idea of the new-generation catalysts should include these three aspects. It is now long known that specific sites are responsible for different molecular reactions taking place on the surface of a supported catalyst. By understanding the molecular interrelations, one may be in a position to manipulate the catalyst's selectivity on an atomic basis. Thus, in order to enhance the reaction selectivity, the nature of the surface sites must be carefully defined and controlled. The catalytic properties of those sites are completely determined by the local electronic structure, and it is therefore a goal by itself to be able to understand and "design" the local electronic structure of the active sites by changing structure and composition of the catalytic materials [1]. One way of modifying the electronic structure of a metallic active site is by adding a second metal, leading, for example, to alloy formation. In this context, nanotechnologies constitute an invaluable tool in the hands of a chemist in order to achieve a multidimensional structural control in the preparation of catalytic systems [2,3]. Whereas some progresses have been accomplished [4–9], in particular in the conception and the modeling of active sites and in the control of the surrounding of these sites, many challenges, which deal with the control of the active site localization and environment at the atomic scale, still exist. Additionally, relatively little investigation has been undertaken in the case of bimetallic catalysts that can present different nanostructures (core–shell, alloy, isolated particles) and for which the control at the atomic scale is even more challenging.

The selective hydrogenation of α, β-unsaturated aldehydes to unsaturated alcohols, which dates back to 1925 [10], has been of growing interest because unsaturated alcohols are important intermediates in the production of fine chemicals and pharmaceutical precursors. This chemoselective hydrogenation is a difficult task, since thermodynamics favor the hydrogenation of the C=C over the C=O bond by ca. 35 kJ/mol and because for kinetic reasons, the reactivity of the C=C bond is higher than that of the C=O bond. Both experimental and theoretical works have been devoted to this topic and comprehensive reviews of the subject have been published [11–14]. In principle, these compounds can be selectively

* Corresponding author.
E-mail address: philippe.serp@ensiacet.fr (P. Serp).

0021-9517/$ - see front matter © 2010 Elsevier Inc. All rights reserved.
doi:10.1016/j.jcat.2010.11.016

hydrogenated by using homogeneous catalysts [15], and promising results have been obtained with colloids [7,8]. However, since such processes required separation steps to recover the target compound, heterogeneous catalysts should be advantageous, being environmentally more friendly and easier to separate and re-use. This is a key aspect for many hydrogenations widely employed in fine chemistry, and developing intrinsically chimio- and regioselective hydrogenation catalysts by tuning the particle morphology and metal-support interaction and by the development of bimetallic formulations is a challenging research field. For supported catalysts, both metal and support influence activity and selectivity of the final catalyst towards the formation of unsaturated alcohols. Metals have different electronic properties, for instance due to their different origin's, exhibiting various properties. It should be pointed out that the final catalyst properties are also a result of specific catalyst pretreatment and that the desired catalyst can be obtained by fine-tuning the catalyst pretreatment procedures [12]. The selectivity to unsaturated alcohols can in general be increased via increasing the number of active sites activating the carbonyl group. Furthermore, several metals or some metal alloys can be used as active components and electronic properties can be tuned by adding promoters [11]. The characteristics of the support material, such as porosity, pore size distribution and reducibility, are also important parameters in catalyst preparation. Besides conventional oxide and activated carbon supports, more advanced support materials, such as carbon nanotubes (CNTs) or nanofibers (CNFs), have been investigated [16–18].

We recently reported high selectivity for the hydrogenation of cinnamaldehyde (CAL) to cinnamyl alcohol (COL) starting from Pt [19,20] and Ir [20] systems supported on CNTs. We also discovered that the use of bimetallic PtRu catalysts deposited on [21] or inside [22] multi-walled carbon nanotubes (MWCNTs) can permit reaching even higher selectivity. For PtRu nanoparticles deposited inside CNTs, confinement effects makes it possible to reach high COL selectivity. When the active phase is deposited on the external surface of MWCNTs, the key step of catalyst design consists in a high temperature treatment under an inert atmosphere. Thus, for monometallic Pt systems, a significant increase in the selectivity is noticed after this treatment, both on CNTs and on CNFs [23], from 10–15% to 60–70%, depending on the support. For the bimetallic PtRu catalysts supported on MWCNTs, the selectivity shifted from 55% to 95% upon thermal activation and this with high conversion levels (80%), placing these catalysts among the best ever reported for this reaction.

To study the effect of this high temperature treatment on the catalytic performances of a bimetallic PtRu catalyst on an inert support material, we made use of MWCNTs, pure and nanostructured materials presenting large pore volume and surface area. Herein, we present a comprehensive study of the preparation and catalytic performance of a series of bimetallic catalysts. Characterization was performed by XPS, WAXS, IR, HTEM, XANES and EXAFS in order to rationalize the structure–properties relationship of these nanocatalysts.

2. Experimental and modeling methods

2.1. Catalysts preparation and characterization

The carbon nanotubes used were prepared from ethylene by catalytic chemical vapor deposition on Fe/Al_2O_3 catalysts [24]. They were purified with an H_2SO_4 treatment and functionalized with an HNO_3 treatment according to a published procedure [25]. Their textural characteristics are given in Table 1. The γ-alumina support, activated, neutral, Brockmann I (particles size: 100–120 μm, BET specific surface area = 155 m^2/g, d = 3.97 g/cm^3 mean pore diameter = 5.8 nm) was purchased from Aldrich. The silica EP10X, BET specific surface area = 310 m^2/g, was provided by Crossfield Limited. The bimetallic PtRu catalysts were prepared from [Pt(COD)Me_2] (1,5-cyclooctadiene)(dimethyl)platinum(II) [26] and [Ru(COD)(COT)] (1,5-cyclooctadiene)(1,3,5-cyclooctatriene)ruthenium(0); the ruthenium precursor was purchased from NanoMePS® (www.nanomeps.fr). In a 250-mL flask, N_2 was bubbled into 60 mL of hexane for 10 min. Under N_2, 2 g of the supporting material was added and well dispersed by 15 min of sonication. Magnetic stirring was allowed and 0.13 g (0.413 mmol) of [Ru(COD)(COT)] and 0.071 g (0.213 mmol) of [Pt(COD)Me_2] were added simultaneously. The mixture was kept at 318 K overnight. Finally, the solid catalytic material (PtRu/CNT623) was obtained by filtration, vacuum drying and reduction in a fixed bed at 623 K under 15 sccm (standard cubic centimeters per minute) of hydrogen and 160 sccm of argon. Further heat treatments were performed under argon on this catalyst at 923, 1123 and 1273 K for 1 h, yielding PtRu/CNT973, PtRu/CNT1123 and PtRu/CNT1273, respectively.

The metal loading of supported metal catalysts was determined by plasma chemical ionization coupled to mass spectroscopy (ICP-MS) after a dissolution step according to sample matrix. The support and catalyst textural characterization was based on the N_2 adsorption isotherms, determined at 77 K with a Coulter Omnisorp 100 CX apparatus. The surface chemistry of the CNT support was characterized by temperature programmed desorption (TPD). TPD experiments were carried out by heating the samples to 1273 K in He flow (60 sccm) at a heating rate of 50 K/min. The amount of evolved gases was recorded as a function of temperature using a quadrupole mass spectrometer (Balzers, model Thermocube). The oxygen content was calculated from the amounts of CO and CO_2 released during the TPD experiments. The hydrogen consumption of the samples was determined by temperature programmed reduction (TPR) performed on 50 mg of sample, in a flow of 3.85% of hydrogen in argon (total flow of 52 sccm). The temperature was increased at the rate of 15 K/min from room temperature to 1173 K.

2.2. Hydrogenation of cinnamaldehyde

A desired amount of catalyst (typically 100 mg) was introduced in a 100-mL autoclave (Top Industrie), and 20 mL of dioxane was added. The autoclave was closed; the stirring was fixed at

Table 1
Chemical and textural characterizations of the catalyst systems prepared for hydrogenation reaction

Catalysts			Catalyst residue						
	Pt (%)	Ru (%)	Fe (%)	Al (ppm)	$d_{average}$ (nm)	D_M (%)	BET (m^2/g)	V_{pores} (cm^3/g)	d_{pore} (nm)
CNT	-	-	0.15	<100	-	-	214	2.16	54
PtRu/CNT623	1.84	2.12	0.13	<100	2.7	47	224	1.6	29
PtRu/CNT973	1.77	2.22	0.46	310	2.9	44	246	2.38	39.33
PtRu/CNT1123	2.88	3.14	0.68	640	6.1	21	-	-	-
PtRu/CNT1273	2.48	2.91	0.20	160	12.9	10	-	-	-
$PtRu/Al_2O_3$	1.94	2.04			2.7	47	147	0.2	6
$PtRu/SiO_2$	1.46	1.68			6.2	21	245	1.7	28

900 rpm and the reactor was purged five consecutive times with H_2 at 0.3 MPa. The reactor was heated to 373 K and kept 2 h under 2 MPa of H_2. Later, it was quickly cooled to 283 K, depressurized and the stirring cut off. The autoclave was opened, the referred amount of CAL was quickly added, and the reactor was closed. The total liquid volume in the autoclave was 40 mL. The autoclave was purged again with H_2 under 900 rpm and heated to the desired temperature. A desired pressure of hydrogen was imposed, and its evolution was followed by a Log 100 program. After the desired time, the autoclave was quickly cooled to room temperature, depressurized, the stirring cut off and the solution recovered. The recovered solution was injected in a gas chromatography apparatus with anisole as internal standard. The catalytic activity was calculated by means of the turnover frequency (TOF) expressed either in moles of cinnamaldehyde transformed per moles of total metal used per second or in moles of cinnamaldehyde transformed per moles of surface metal used per second. The surface dispersion of the PtRu particles was calculated using Eq. (1) ponderated from the metal loadings and assuming an equal distribution of both metals in the particles:

$$D_M = (6n_sM)/(rNd_p) \quad (1)$$

where n_s is the number of atoms at the surface per unit area ($1.12 \times 10^{19}/m^2$ for Pt and $1.63 \times 10^{19}/m^2$ for Ru), M is the molar mass of the metals (195.084 g/mol for Pt and 101.07 g/mol for Ru), r is the density of the metals (21.45×10^6 g/m^3 for Pt and 12.1×10^6 g/m^3 for Ru), N is the Avogadro number (6.023×10^{23} at/mol) and d_p is the average particle size (determined by HRTEM, assuming that particles are spherical). The selectivity towards cinnamyl alcohol was calculated relative to the main hydrogenation products, i.e. hydrocinnamyl alcohol and hydrocinnamaldehyde.

2.3. High resolution transmission electron microscopy

The HRTEM results were obtained using a 200 kV JEOL JEM-2100F microscope, equipped with a field emission gun. The microscope can also operate in STEM mode, when the electron beam forms a 1-nm-diameter probe, and this mode was used with scanning of the probe to collect EDX spectra. For EDX spectra, the typical probe current was approximately 2 nA, and the typical collection time was 30 s. The EDX detector was a Princeton Gammatech LS30135 Si(Li) detector with ultrathin window, and had a uniform response in the range 3–20 keV and a resolution of 135 eV at 5.9 keV.

2.4. Wide angle X-ray scattering study of PtRu samples

Data were collected on an X-ray powder diffractometer dedicated to the study of less ordered materials, characterized by a relatively high energy source (Molybdenum anode, 0.071069 nm wavelength) and low background. A small amount of powdered sample was sealed in Lindemann glass capillaries of 1.5 mm diameter (samples PtRu/CNT623, PtRu/CNT973, PtRu/CNT1123 and PtRu/CNT1273); pure carbon nanotubes were also similarly prepared and measured under the same conditions to allow for matrix subtraction. All data sets included 457 points equally spaced in k-space ($k = 4 * \mathrm{pi} * \sin(\theta)/\lambda$); the 2θ range was 0–129°; measurement time was 150 s per point for all samples.

Classic polarization and absorption corrections were applied. After subtraction of the contribution of pure nanotubes, the data were normalized and then Fourier transformed in order to obtain the radial distribution function (RDF, also called pair distribution function). The RDF displays a series of peaks pointing to distances between pair of atoms, up to the coherence length. The complete damping of the function is related, for well-ordered objects, to the size of the particles. However, because of the limited resolution of the instrument, the function is terminated for distances between 4 and 5 nm. Peaks amplitude depends on many factors: multiplicity of the distance, which is itself related to the average number of atoms, size of the particles, and static disorder in the structure.

A critical step in data reduction was the accurate determination of the matrix amount (pure CNTs) to be subtracted: very small changes in capillary diameter or sample density have a strong influence, thus excluding *a priori* correction. A simple criterion was used: the cancellation, in reciprocal space, of peaks characteristic of CNTs (e.g. peak at $2\theta = 10°$); an additional criterion was the cancellation, in real space, of the characteristic C—C distance. Non-corrected diffractograms are shown in Supporting information.

2.5. X-ray absorption spectroscopy data collection (EXAFS and XANES)

EXAFS and XANES data were collected in transmission mode at beamline 11.1 (XAFS) at the ELETTRA synchrotron, Trieste (Italy). Spectra at the Ru K-edge (22117 eV) and Pt L_{III}-edge (11564 eV) were acquired at room temperature using a Si(3 1 1) monochromator. Data were collected on samples PtRu/CNT623 and PtRu/CNT973 and on Ru and Pt reference samples (RuO_2, Ru, $Na_2Pt(OH)_6$, Pt). Samples with a suitable and highly uniform optical thickness were prepared from powders, apart from the Pt metal reference which was in the form of a foil. In the case of RuO_2 and Na_2PtOH_6, the powders were dispersed in ethanol and then filtered onto polyethylene supports. The samples and the Ru metal reference were prepared as pellets by diluting the powder in PVP; pellets were made inside a glove-bag to reduce contact with air.

2.5.1. EXAFS and XANES data analysis

The EXAFS data were analyzed using the program Viper to sum the data, identify the beginning of the absorption edge, E_o, fit pre- and post-edge backgrounds, and hence to obtain the normalized absorbance χ as a function of the modulus of the photoelectron wavevector k^3 [27]. The modular package DL_EXCURV [28], based on the EXCURV98 code, was used in the final stage of data processing to model the experimental $\chi(k)$ in order to extract structural information. This code uses fast curved wave theory [29] and calculates *ab initio* the effective curved wave backscattering amplitude of the scatterer, the phase shift due to the absorbing atom potential, the phase shift due to the scatterer, and the inelastic mean free path of the photoelectron [30,31]. The structural parameters were obtained by nonlinear least squares fitting in k-space with a k^3 weighting to emphasize the high-energy part of the spectrum. The fitting was carried out using the k range 2.5–16 Å^{-1}. Fourier transform (FT) of EXAFS data corrected for phase-shift shows peaks that correspond to local atom correlations. The positions of the peaks (R) correspond to bond distances between the central and the backscatterer atoms.

The errors in the fit parameters were obtained from the 95% confidence level, as calculated in EXCURV98. The number of fitted parameters was always less than the number of statistically independent data points, as estimated in the standard way [32]. The quality of the fit was judged from the normalized sum of residuals:

$$R\text{-factor} = \sum_n k_n^3 \left|\chi_{\mathrm{expt}}(k_n) - \chi_{\mathrm{fit}}(k_n)\right| \Big/ \sum_n k_n^3 |\chi_{\mathrm{expt}}(k_n)| \times 100 \quad (2)$$

Reasonable EXAFS fits of single shells typically have values of R-factor around 20%; however, when the fit is performed on the total EXAFS spectra, higher values of R-factor can still correspond to good fits especially if the fit is not extended to peaks at high R.

The XANES spectra were processed in the usual way to obtain normalized absorbance [33]. XANES at the K-edge involves the

excitation of a 1s photoelectron into low-lying empty states at the central atom with p-type symmetry. XANES at the L_{III}-edge represents $p_{3/2} \rightarrow d_{3/2}$ and $d_{5/2}$ transitions.

The XANES spectra have been analyzed qualitatively using the "fingerprint" method, by comparing spectra from samples with those from reference compounds.

2.6. Computational details

In the present work, we carried out Density Functional Theory (DFT) calculations using the Vienna *ab initio* simulation package (VASP) [34]. The code uses the full-potential Projector Augmented Waves (PAW) framework [35]. Exchange–correlation effects have been approximated using the PBE [36] functional and applied in spin-polarized calculations. A kinetic energy cutoff of 400 eV was found to be sufficient to achieve a total energy convergence within several meV considering *k*-point sampling. All atoms were fully relaxed to forces on individual atoms smaller than 0.02 eV/Å. Considering the smearing issue, during the geometry's optimization runs, a Gaussian smearing was applied with a width of 0.2 eV, while the tetrahedron method with Blöchl corrections [37] was used for accurate energy calculations. Diffusion barriers were estimated by the climbing image nudge elastic band (CI-NEB) method [38], with a force tolerance of 0.02 eV/Å and five intermediate geometries for the transition state search.

To model the nanotube's sidewall with large diameters, we used one single flat graphene layer (98 C atoms in total) in a slab supercell calculation with 18.3 Å of vacuum in the *c* direction. It ensures no reciprocal interaction between periodic images in this particular direction. Moreover, to study the effect of curvature on adsorption's energies, we used a (6, 6) tube, modeled by five primitive cells, for a total of 120 C atoms, with a vacuum of around 14 Å between repeated images of the CNT.

3. Results

3.1. Hydrogenation catalysts

Catalysts of 2–2 wt.% Pt–Ru/support were elaborated from the [Pt(COD)Me_2] and [Ru(COD)(COT)] organometallic precursors in hexane at 318 K under Ar, and reduced at 623 K under a 10% H_2/Ar mass flow. Before impregnation, the purified CNT support was activated by oxidative nitric acid oxidation to create significant amounts of surface oxygenated groups, acting as nucleation centers for precursor anchoring [19]. The concentration of surface —COOH groups was 0.011 mmol/g, as determined by chemical titration. Porous alumina and silica supports were also used for comparison purposes. The PtRu/CNT623 sample was then heat treated under argon at 973, 1123, or 1273 K, in order to eliminate the oxygenated surface groups of the support [19], and to induce sintering. Indeed, it is known that large particle size favors the hydrogenation of the C=O bond [11]. The catalysts thus produced were named PtRu/CNT973, PtRu/CNT1123 and PtRu/CNT1273, respectively. Chemical and textural characterizations of the catalysts are presented in Table 1.

The metal loading measured was relatively close to the expected value for CNT and alumina, and slightly lower for the silica support, presumably because of the lower amount of oxygenated groups (silanol) on this latter support. Indeed, typical values for oxygenated groups range between 10 and 15 –OH/nm^2 for alumina, 2 and 6 –OH/nm^2 for silica [39], and a value of 7.2 O/nm^2 has been extracted from TPD data for the activated CNT support. TEM indicates that the particle–size distribution is rather narrow for PtRu/CNT623 and PtRu/Al_2O_3, while some large (20–50 nm) particles coexist with small (2–5 nm) ones for PtRu/SiO_2. For the heat-treated samples (Fig. 1), no significant variation in the mean particle size is noticed up to 973 K, pointing out the high thermal stability of this catalyst. Then, a significant sintering occurs between 973 and 1273 K, with the appearance of a bimodal particle size distribution (see Supporting information SI1).

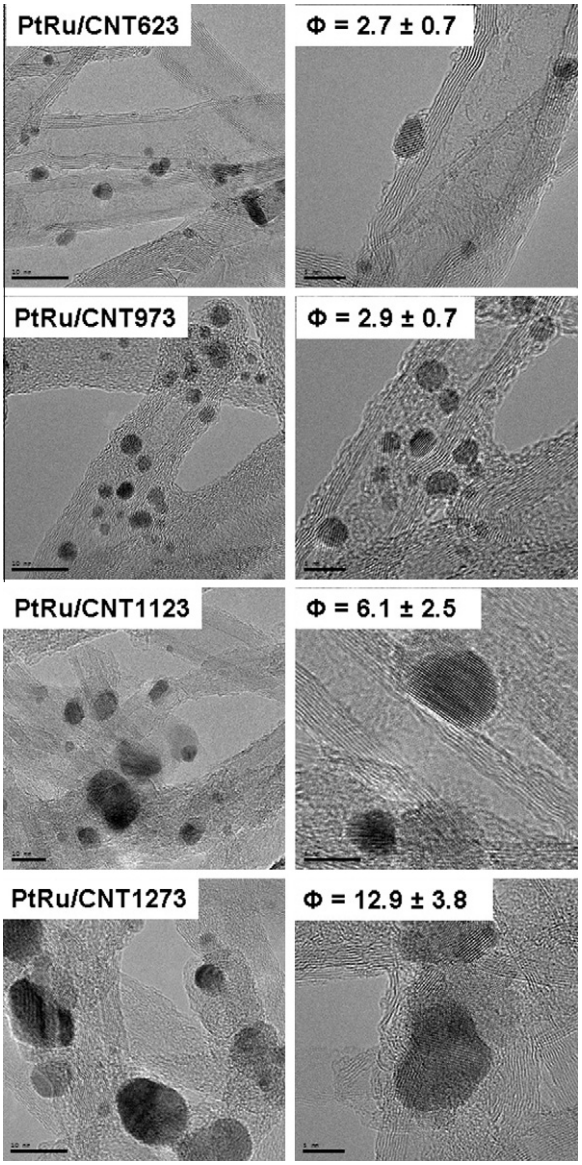

Fig. 1. Low-magnification HRTEM images of the PtRu/CNT samples (left scale bar = 10 nm, and right scale bar = 5 nm).

3.2. Hydrogenation of cinnamaldehyde over PtRu/CNT

The hydrogenation of cinnamaldehyde may proceed via different reaction pathways. The 1,2-addition of hydrogen gives the unsaturated alcohol (COL). The 3,4-addition gives the saturated aldehyde (HCAL). The hydrogenation of the C=O and C=C bonds gives the saturated alcohol (HCOL). This reaction scheme can be further complicated considering side reactions such as decarbonylation, isomerization, and hydrogenolysis reactions leading to by-product formation. The use of alcoholic solvents and the presence of acid/basic sites on the catalyst's surface favors the formation of by-products. The present study was performed in dioxane in order to avoid by-product formation. The catalytic performances of the different systems are presented in Table 2.

Table 2
Performances of the catalytic systems for the hydrogenation of cinnamaldehyde.

Catalysts	Conversion (%)	TOF [a] (s^{-1})	TOF [b] (s^{-1})	Selectivity (%)		
				COL	HCOL	HCAL
CNT	9	–	–	69	19	12
PtRu/CNT623	72	0.21	0.099	53	18	29
PtRu/CNT973	67	0.21	0.091	78	11	11
PtRu/CNT1123	82	0.36	0.075	86	9	4
PtRu/CNT1273	78	0.79	0.079	94	3	3
$PtRu/Al_2O_3$	24	0.07	0.033	52	12	36
$PtRu/SiO_2$	24	0.20	0.042	65	4	31

[a] Expressed in moles of cinnamaldehyde transformed per moles of surface metal used per second.
[b] Expressed in moles of cinnamaldehyde transformed per moles of total metal used per second.

First, the selectivity to cinnamyl alcohol was affected by the nature of the support. At a first glance and not taken into account the heat-treated samples, we can say that the best selectivity towards COL was achieved with the silica supports, SiO_2 > Al_2O_3 ~ CNTs. However, as it has been reported that the selectivity to cinnamyl alcohol increases as the particle size increases [40], the higher selectivity achieved with the $PtRu/SiO_2$ catalyst should be attributed to the larger particle size observed for this system ($d_{average}$ = 6.2 nm) compared to the alumina ($d_{average}$ = 2.7 nm) and CNT supports ($d_{average}$ = 2.7 nm). This is attributed to a steric effect whereby the planar cinnamaldehyde molecule cannot adsorb parallel to a flat metal surface because of the steric repulsion of the aromatic ring. Indeed, theoretical calculations showed that aromatic rings that are chemisorbed on a metal surface must lie at a distance exceeding 0.3 nm because there is an energy barrier preventing a closer approach to the surface [40]. Because of this energy barrier, the C=C bond cannot approach the surface as closely as the C=O bond does, the latter being then hydrogenated preferentially. This steric effect does not operate on small particles, where both the C=C and the C=O bonds can approach the surface. In addition, SiO_2 presents surface groups that act as electron-donor sites modifying the electronic properties of the nanoparticles and increasing selectivity. Considering now the different catalysts on MWCNTs, the selectivity towards cinnamyl alcohol increased linearly with the activation temperature to reach 94% for PtRu/CNT1273. This impressive increase in selectivity cannot be the result of the increase in particle size only. Indeed, Fig. 2a, which presents the influence of nanoparticle size on the selectivity for the Pt–Ru/CNT catalysts, shows that two effects should coexist: first, a pronounced structural effect that may result from the heat treatment and secondly the size effect. If we are now considering the effect of the heat treatment on the catalytic activity of the Pt–Ru/CNT catalysts, surprisingly we noticed a significant increase in the TOF with the metal particle size (Fig. 2b).

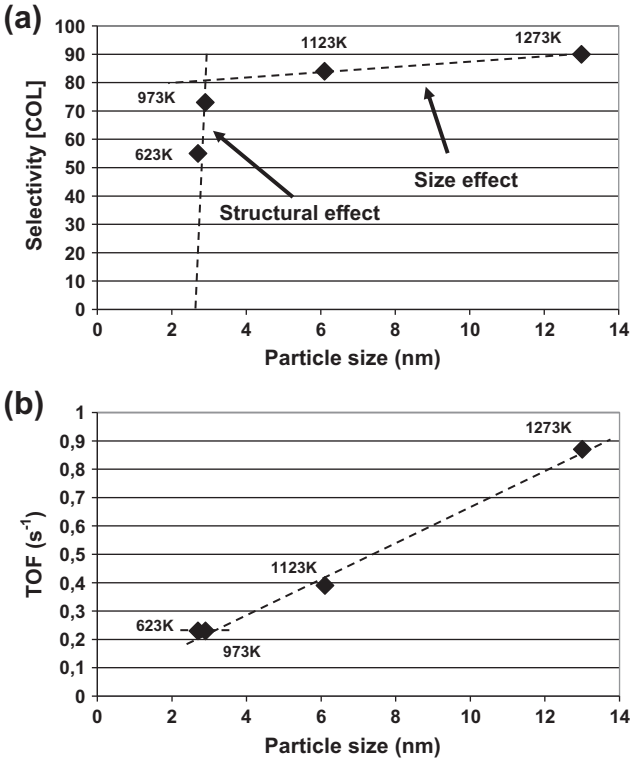

Fig. 2. Effect of the particle size on (a) the selectivity towards COL and (b) the turnover frequency.

3.3. Catalyst characterization

3.3.1. High resolution transmission electron microscopy

3.3.1.1. Sample PtRu/CNT623. The high resolution transmission electron microscopy (HRTEM) analysis of the sample PtRu/CNT623 shows the coexistence of two separate crystalline phases. The first one has a face-centered cubic (fcc) structure typical of Pt, while the second one has a hexagonal close packed (hcp) structure characteristic of Ru. In Fig. 3 an HRTEM image of PtRu/CNT623 sample is reported. Two distinct particles are here clearly visible, labeled (a) and (b), both oriented to show a structural projection. The insets show the numerical diffractogram of the two particles, obtained on the base of the two-dimensional fast Fourier transform (2D-FFT) calculated over the square zones reported in the HRTEM image. The particle labeled (a) shows a structural projection that can be ascribed to an fcc lattice oriented along its [0 0 1] zone axis. The interplanar distances measured for the two perpendicular sets of lattice planes are both equal to 1.89 Å. It is likely that these distances were originally those corresponding to two mutually perpendicular (2 0 0) lattice set of planes for pure platinum that should measure 1.96 Å. Therefore, the measured distance indicates a compressive strain (i.e., a contraction of the original lattice) for the platinum fcc structure, due to a certain number of Ru atoms diffusing into the Pt lattice. In particular, the observed cubic lattice appears contracted of −3.7% with respect to that of the pure bulk platinum. The particle labeled (b) shows a different structure. It seems not too far from that expected for a hcp lattice oriented along its [1 0 0] zone axis, with some differences in the interplanar distances with respect to those of the pure hcp Ru.

More specifically, if one compares the measured structure with that of the pure hcp ruthenium, it is possible to observe that:

(a) all the interplanar distances are larger than those expected for pure ruthenium, indicating a tensile strain (i.e., a dilatation of the original lattice) of the original pure Ru lattice; and
(b) the tensile strain is not the same for the different crystalline axis. In fact, the original Ru (002) distance of 2.14 Å slightly increases to 2.16 Å. On the contrary, the two other pairs of

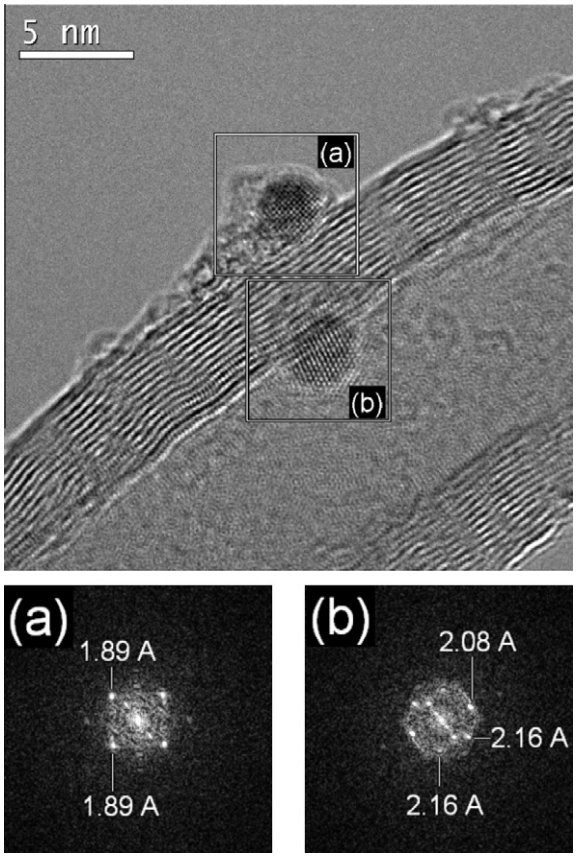

Fig. 3. HRTEM image of the sample PtRu/CNT623. A CNT is clearly observed together with two small particles, surrounded by a square labeled (a) and (b), respectively. The insets (a) and (b) show the numerical diffractogram of the corresponding square regions: the distance measured for each set of lattice planes is also reported.

spots in the numerical diffractogram, corresponding to two *d*-equivalent (1 0 1) lattice sets (d = 2.06 Å for the pure ruthenium), show a quite different increase in their respective directions: 2.08 Å (+1% with respect to pure ruthenium) for the one that is counterclockwise with respect to the (0 0 2) spots, and 2.16 Å (+4.8%) for the one that appears clockwise. Besides, the angles around the (0 0 2) direction are almost equal to those expected for the hcp structure in its [1 0 0] zone axis, the small differences observed being inside the intrinsic angular error due to a measurement taken out on a numerical diffractogram calculated over a small area of the HRTEM image. The basic hcp character seems then retained, but a lattice tensile strain is present. This could be ascribed to the fact that a certain number of Pt atoms have diffused in the Ru lattice.

Finally, even if – in the case of local compositional/phase differences – the HRTEM analysis has low statistically informative value, it was observed that in the sample PtRu/CNT623, the small particles have the tendency to have the fcc structure while the bigger ones tend to adopt a hcp structure.

3.3.1.2. Sample PtRu/CNT973. The HRTEM analysis of the sample PtRu/CNT973 mainly shows crystalline particles with similar structure to that reported in Fig. 3a. An HRTEM image of PtRu/CNT973 sample is reported in Fig. 4a. The inset shows the numerical diffractogram of the particle. The latter shows a structure that can be most likely ascribed to an fcc lattice oriented along its [0 1 1] zone axis. The interplanar distances measured for the four sets of lattice planes are equal to 2.10 Å, 1.87 Å, 2.13 Å, 1.25 Å, and the angular distances between them are those expected for an fcc lattice in its [0 1 1] zone axis. These should then correspond to the (1 1 –1), (2 0 0), (1 –1 1) and (0 –2 2) lattice sets, respectively. If one compares these *d*-values with those expected for the pure platinum fcc structure (d(1 1 1) = 2.26 Å, d(2 0 0) = 1.96 Å and d(0 2 2) = 1.39 Å), it is interesting to note that a compressive strain of the lattice is observed once again. However, in this case, the contraction is much more pronounced than in the case of the sample PtRu/CNT623, and the value is not the same for the different fcc lattice planes. In fact, it is maximized along the (0 –2 2) axis (−9.1% with respect to the corresponding axis of the pure platinum) and minimized along the (2 0 0) one (−4.8%), perpendicular to the (0 –2 2). Besides, a contraction is observed along the (1 1 –1) and (1 –1 1) axis, which is slightly different for the two axis (around −7% in average). Even in this case, the phenomenon is probably due to the diffusion of Ru atoms in the original Pt lattice upon heat treatment.

3.3.1.3. Sample PtRu/CNT1123. The HRTEM analysis of the sample PtRu/CNT1123 shows, again, a crystalline configuration similar to that reported in the previous Figs. 3a and 4a. In Fig. 4b an HRTEM

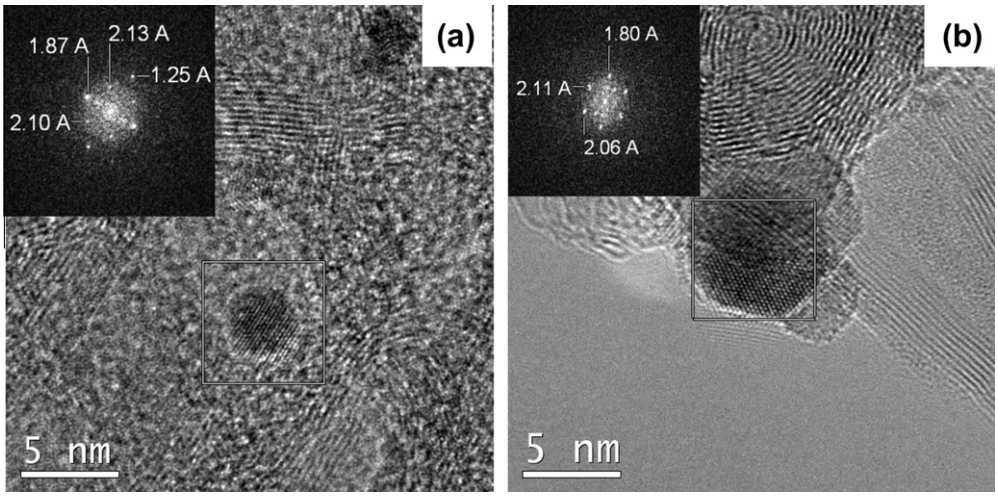

Fig. 4. HRTEM images of the sample PtRu/CNT973 (a) and PtRu/CNT1123 (b). In each image, a particle is surrounded by a square. The insets show the numerical diffractogram of the square region; the distance measured for each set of lattice planes is also reported.

image of PtRu/CNT1123 sample is reported. The inset shows the numerical diffractogram of the particle. It shows a structure that most likely can be, again, ascribed to an fcc lattice oriented along its [0 1 1] zone axis. The interplanar distances that are measured for the three sets of lattice planes are respectively equal to 2.11 Å, 1.80 Å, and 2.06 Å, and the angular distances between them are those expected for an fcc lattice in its [0 1 1] zone axis. These should then correspond to the (1 1 –1), (2 0 0), and (1 –1 1) lattice sets, respectively.

If one compares these *d*-values with those expected for the pure platinum fcc structure, a compressive strain of the lattice is again observed. However, in this latter case, the contraction further evolved with respect to the sample PtRu/CNT973. Here, the compressive strain is −8.8% with respect to the corresponding axis of the pure platinum along the (2 0 0) axis. Besides, a contraction is observed even along the (1 1 –1) and (1 –1 1) axis, which is slightly different for the two axes (−8.3% in average). Also, in this case, the observed changes on the lattice are likely due to the diffusion of Ru atoms in the original Pt lattice.

An EDS quantification was also performed for samples PtRu/CNT623, PtRu/CNT973 and PtRu/CNT1123. The quantification was done using the Cliff–Lorimer method. The atomic fraction of each element C_A and C_B can be related to the measured intensities by the so-called Cliff–Lorimer equation

$$\frac{C_A}{C_B} = k_{AB}\frac{I_A}{I_B}$$

where *A* is Pt and *B* is Ru. I_A and I_B are the heights of the corresponding Gaussians for the peaks used in the fit. The background was approximated with an exponential function. The variable k_{AB} is the calculated Cliff–Lorimer factor (=0.631 at 200 kV). For each sample, a total spectrum was calculated by summing all the single particle spectra (this approximates an average for particles with similar size). The corresponding data are reported in Supporting information (SI2). As shown in Table 3, there is a clear trend in the Pt/Ru ratio with increasing temperature (Pt decreases).

3.3.2. Wide angle X-ray scattering

The diffractograms of the four samples PtRu/CNT623–1273 are shown in Fig. 5a after correction for self-absorption and contribution from nanotubes. Several observations can be made from this figure, in particular focusing on the range including the peaks characteristic of the fcc and hcp structures:

- before heat treatment (PtRu/CNT623), small and broad peaks indicating small objects; in good agreement with an fcc pattern (18.3°, 21.1° in 2θ); for a good agreement, the pattern must, however, be adjusted according to a cell parameter 1.5% smaller than in pure Pt;
- after heat treatment at 973 K, the pattern also includes hcp features (19.6°, 25.7° in 2θ);
- both fcc and hcp peaks are also observed in PtRu/CNT1123, but peaks are much sharper, indicating much larger and/or less disordered particles;
- for PtRu/CNT1273, a pattern similar to PtRu/CNT1123 is obtained, with however a reduction – however, with a reduction in sharpness.

Table 3
Ru and Pt concentration as a function of temperature obtained from the fits of the EDX spectra.

T (K)	Pt at.%	Ru at.%
623	62 (±3)	38 (±2)
973	44 (±2)	56 (±2)
1123	39 (±1)	61 (±1)

Similar observations can be made in real space (Fig. 5b). RDF amplitudes are similar for PtRu/CNT623 and PtRu/CNT973, indicating similar sizes, while a dramatic increase occurs for PtRu/CNT1123, followed by a small reduction for PtRu/CNT1273. Coherence length can be evaluated to be 2.5 nm for PtRu/CNT623, and 3.0 nm for PtRu/CNT973; however, a similar estimation cannot be made for PtRu/CNT1123 and PtRu/CNT1123 because of the limited resolution of the instrument: the extinction of the functions above 4 nm only indicates that their size is at least equal to 4 nm. These data fit perfectly with the TEM analyses (Table 1).

To identify the fcc or hcp characters, it is interesting to focus on the 0.8–1.0 nm range (Fig. 5b inset), which is very different for the two structures: PtRu/CNT623 is nearly purely fcc, whereas both characters appear for the three heat-treated samples.

Because PtRu/CNT623 is very close to the perfect fcc structure (SI4), an accurate comparison with an adjusted fcc model is possible: a good agreement is obtained for a 2.4-nm particle, applying a 1.5% shrinking factor to the pure Pt parameter. The resulting a parameter for the cubic cell is 0.3865 nm, which points to a Ru content slightly smaller than 50% [41].

To investigate the effect of oxidation, the glass capillaries were opened and the four samples were re-measured after short (1 h) and long (approximately 1 month) exposure to air. The main result is that samples PtRu/CNT973, PtRu/CNT1123 and PtRu/CNT1273 displayed nearly no evolution from the diffraction point of view, even after being exposed to air for 1 month. Quite differently, sample PtRu/CNT623 presents clear indications of oxidation just after one hour and a very strong alteration after one month (SI5). Since oxidation affects Ru atoms much more than Pt ones, this result is consistent with a very different exposition of Ru atoms in PtRu/CNT623 compared to the three other samples where they are likely much more protected.

3.3.3. XANES and EXAFS results

In Fig. 6, the XANES spectra of PtRu/CNT623 and PtRu/CNT973 samples are compared with those of the reference samples. The spectra at the Pt L_{III}-edge indicate that Pt is mostly present as Pt^0 in both samples, with just a hint of the presence of Pt in a higher oxidation state in PtRu/CNT623, while the Ru K-edge spectra suggest a much higher content of oxidized Ru in both samples. Finally, the Ru is less oxidized in PtRu/CNT973 sample compared to PtRu/CNT623, which is coherent with the WAXS results.

The EXAFS interference functions $k^3\chi(k)$ at the Ru K-edge and Pt L_{III}-edge of samples PtRu/CNT623 and PtRu/CNT973 along with the reference samples are shown in Fig. 7. The corresponding FTs are shown in Fig. 8.

At the Ru K-edge, the EXAFS interference functions $k^3\chi(k)$ of PtRu/CNT623 and PtRu/CNT973 show significant differences. In particular, the $k^3\chi(k)$ of PtRu/CNT623 shows very weak oscillations at high *k*, indicating a very disordered and/or poorly symmetric structure; because of the weak oscillations, the noise is quite noticeable. The differences between the two samples are also evident in the corresponding FTs; in particular, the peak around 2.5–3 Å, which is due to Ru bonded to either Ru or Pt, is increasing significantly going from PtRu/CNT623 to PtRu/CNT973. In both samples, evidence of a contribution of Ru bonded to a light element (either O or C) at about 2 Å is also present. No peak beyond 3 Å is evident.

At the Pt L_{III}-edge the EXAFS interference functions $k^3\chi(k)$ of PtRu/CNT623 and PtRu/CNT973 are much more similar, showing oscillations with similar amplitudes. The comparison of the FTs of the samples with those of the reference compounds suggests also, in this case, the presence of a contribution of Pt bonded to a light element (O or C) together with a contribution from Pt bonded

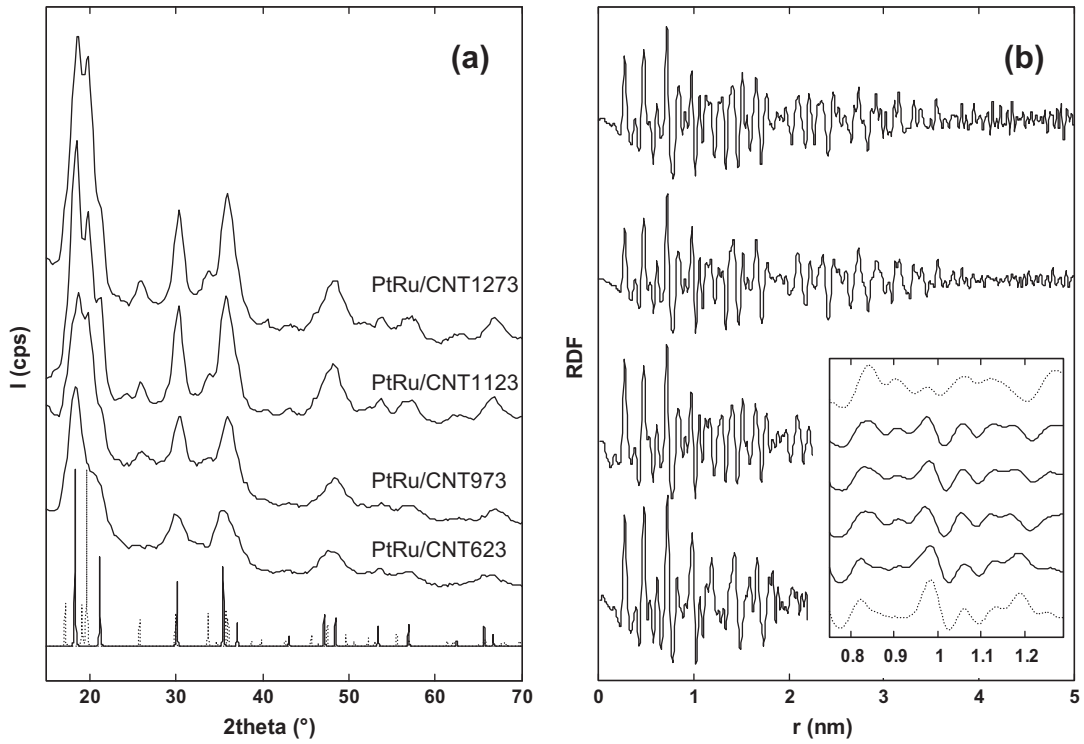

Fig. 5. (a) Corrected diffractograms of all four samples, with hcp Ru (dotted line) and fcc Pt (solid line, adjusted for 1.5% shorter cell parameter) references, (b) related RDFs in same order (for easier comparison, amplitudes have been divided by three for PtRu/CNT1123 and two for PtRu/CNT1273); inset: close-up of RDFs, with references in dotted line (top: Ru structure, bottom: Pt structure contracted by 1.5%).

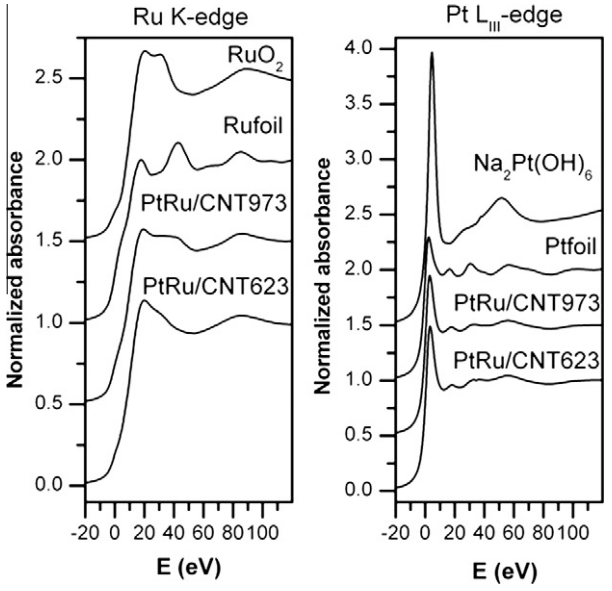

Fig. 6. XANES Spectra at Ru K-edge and Pt L_{III}-edge for PtRu/CNT623 and PtRu/CNT973 compared with reference compounds.

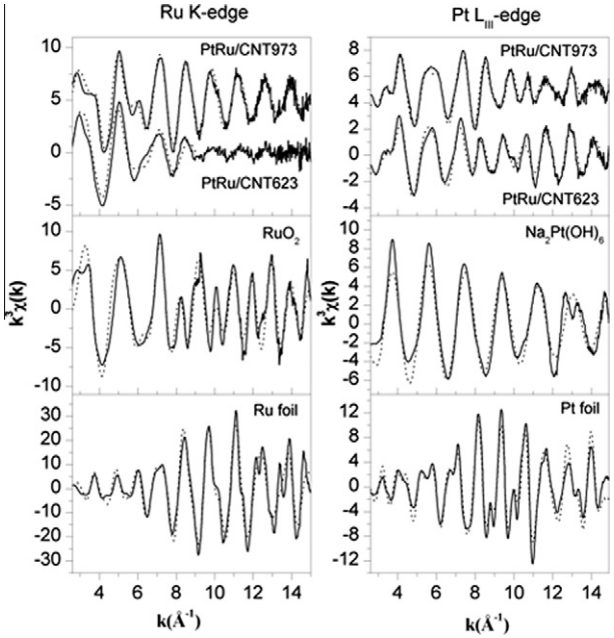

Fig. 7. EXAFS interference functions $k^3\chi(k)$ at the Ru K-edge and Pt L_{III}-edge for PtRu/CNT623 and PtRu/CNT973 samples, and for reference compounds.

to a heavy element (Ru or Pt). In PtRu/CNT973, a peak beyond 3 Å is also evident.

The qualitative analysis of the EXAFS interference functions and corresponding FTs indicates that fitting requires at least one shell involving a light element and one involving a heavy element. Due to the stronger backscattering of heavy elements, it is more difficult to distinguish between O or C neighbors than to distinguish between Ru or Pt neighbors. Even if some contributions from Ru–C interactions cannot be ruled out, the fitting of the two samples at the Ru K-edge was performed considering only O in the first shell, since it is well known that Ru is easily oxidized. Moreover, XANES data indicate that Ru is partly oxidized in both samples and that PtRu/CNT623 sample is more oxidized than PtRu/CNT973. At the Pt L_{III}-edge, the presence of Pt–O interactions is more questionable and in fact XANES data indicate very little oxidation in both samples, with PtRu/CNT623 sample slightly more

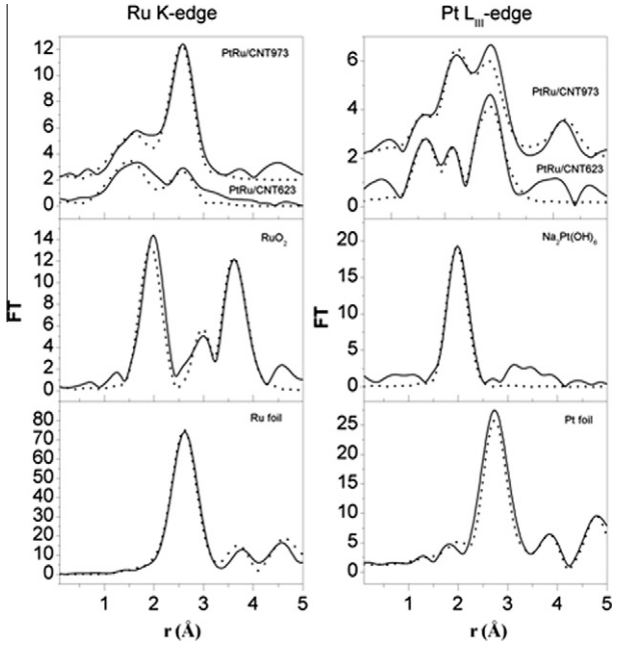

Fig. 8. FTs at the Ru K-edge and Pt L_{III}-edge for PtRu/CNT623 and PtRu/CNT973 samples, and for reference compounds.

oxidized than PtRu/CNT973. In this case, the fitting of the first shell was done considering either Pt–O interactions or Pt–C interactions, obtaining quite similar results. For the sake of simplicity, only the results obtained considering Pt–O interactions will be presented.

The *ab initio* phase shifts and amplitudes calculated in DL_EXCURV were first used to fit the data of the reference samples. Good fits (shown in Figs. 7 and 8, best-fit parameters reported in Tables 4 and 5 for the Ru K-edge and Pt L_{III}-edge respectively) were obtained considering only single scattering contributions for Ru, RuO_2 and Na_2PtOH_6 reference samples, while multiple scattering contributions were also taken into account for Pt foil, since some multiple scattering path are expected to be strong due to a forward-scattering (also called the focusing or shadowing effect) consisting of collinear arrangements of neighboring atoms [42]. Coordination numbers were kept fixed to the values of the known crystal structures, while distances and Debye–Waller factors were fitted, together with EF which is a correction to the beginning of the absorption edge, E_o.

In the fitting of the samples, coordination numbers were also free to vary, in addition to distances, Debye–Waller factors and EF. Best fits for PtRu/CNT623 at the Ru K-edge (shown in Figs. 7 and 8, best-fit parameters reported in Table 4) were performed with one Ru–O shell and one Ru–Ru shell. The fit did not improve with the addition of another Ru–Pt shell. The R-factor is high, due to very noisy data.

A good fit was obtained for the same sample at the Pt L_{III}-edge with a first shell of either Pt–O (fit shown in Figs. 7 and 8, best-fit parameters reported in Table 5) or Pt–C, as already discussed, and a second shell involving both Pt–Ru and Pt–Pt interactions. Shells involving both heavy atoms had to be introduced in order to get a good fit, suggesting the formation of an alloy.

The best fit of PtRu/CNT973 at the Ru K-edge (shown in Figs. 7 and 8, best-fit parameters reported in Table 4) was obtained with one Ru–O shell and an additional shell with both Ru–Ru and Ru–Pt, to take into account the second peak in the FT. In this case, the presence of additional Ru–Pt interactions improved the fit significantly enough to justify the use of additional free parameters.

The best fit of PtRu/CNT973 at the Pt L_{III}-edge, similarly to PtRu/CNT623, was obtained with a first shell of either Pt–O (fit shown in Figs. 7 and 8, best-fit parameters reported in Table 5) or Pt–C, a second shell involving both Pt–Ru and Pt–Pt interactions and an additional shell involving only Pt–Ru. Since there is a clear evidence of the formation of an alloy, also this latter shell should include both Ru–Ru and Ru–Pt interactions. However, only one contribution was considered in order to limit the number of free parameters.

The results of the fitting clearly indicate that the structural evolution of the Ru environment with the temperature of the thermal treatment is slower than that of the Pt environment, since the Ru environment of PtRu/CNT623 is significantly different from that of PtRu/CNT973 while the Pt environment is quite similar in PtRu/CNT623 and PtRu/CNT973. The results also indicate that the alloying process is progressing with the temperature of the thermal treatment.

The coordination number for Ru–Ru(Pt) and Pt–Pt(Ru) in the samples are significantly smaller than the value of 12 found in the pure metals. The reduction in coordination number is due to two concomitant effects; the fact that some Ru, and in a much minor extent some Pt, is bonded to O (or C) and to the dimension of the nanoparticles. A reduction of coordination numbers is expected for nanocrystals smaller than 5 nm [43], and the reduction becomes progressively more significant for outer shells as the crystallite size decreases. The effect of the reduced nanocrystal size is also detectable from the absence of shells beyond 3 Å in PtRu/CNT623 and 4 Å in PtRu/CNT973.

4. Discussion

The bimetallic PtRu catalysts have been prepared from two organometallic precursors, [Pt(COD)Me_2] and [Ru(COD)(COT)], the reductive decomposition of which leads to pure metal at moderate temperatures [22]. We noticed that although it is possible to deposit the ruthenium precursor at 318 K on CNTs, no surface reaction occurs at this temperature when starting from [Pt(COD)Me_2]. Therefore, the deposition of [Ru(COD)(COT)] on surface oxidized CNTs occurs at lower temperature than that of [Pt(COD)Me_2]. The effective co-deposition of platinum and ruthenium at 318 K thus involves that ruthenium deposits first and that the grafted

Table 4
Interatomic distances (R), coordination numbers (N) and Debye–Waller factors (σ) obtained from fitting data of samples and of reference compounds at the Ru K-edge.

Ru K-edge															
Ru Foil				RuO_2				PtRu/CNT623				PtRu/CNT973			
	R (Å)	N	$2\sigma^2$		R (Å)	N	$2\sigma^2$		R (Å)	N	$2\sigma^2$		R (Å)	N	$2\sigma^2$
Ru–Ru	2.67(1)	12	0.011(1)	Ru–O	1.97(1)	6	0.015(1)	Ru–O	2.00(1)	4.3(3)	0.033(3)	Ru–O	1.97(2)	2.5(2)	0.025(3)
Ru–Ru	3.78(1)	6	0.011(1)	Ru–Ru	3.07(1)	2	0.011(3)	Ru–Ru	2.65(1)	3.0(7)	0.036(5)	Ru–Ru	2.65(1)	3.5(3)	0.017(1)
Ru–Ru	4.27(1)	2	0.014(2)	Ru–O	3.42(3)	4	0.018(2)					Ru–Pt	2.67(1)	1.5(6)	0.018(4)
Ru–Ru	4.67(1)	18	0.014(1)	Ru–Ru	3.54(1)	8	0.014(1)								
Ru–Ru	5.33(1)	12	0.015(1)	Ru–O	3.85(1)	12	0.020(5)								
R-factor = 33				R-factor = 35				R-factor = 45				R-factor = 29			

Table 5
Interatomic distances (R), coordination numbers (N) and Debye–Waller factors (σ) obtained from fitting data of samples and of reference compounds at the Pt L_{III}-edge.

Pt L_{III}-edge															
Pt foil				Na_2PtOH_6				PtRu/CNT623				PtRu/CNT973			
	R (Å)	N	$2\sigma^2$		R (Å)	N	$2\sigma^2$		R (Å)	N	$2\sigma^2$		R (Å)	N	$2\sigma^2$
Pt–Pt	2.77(1)	12	0.016(1)	Pt–O	2.01(1)	6	0.005(1)	Pt–O	2.00(1)	1.4(1)	0.015(2)	Pt–O	2.00(1)	1.2(1)	0.024(4)
Pt–Pt	3.91(1)	6	0.016(1)					Pt–Ru	2.69(1)	1.2(3)	0.018(2)	Pt–Ru	2.69(1)	1.8(2)	0.016(1)
Pt–Pt	4.81(1)	24	0.018(1)					Pt–Pt	2.74(1)	4.3(3)	0.018(1)	Pt–Pt	2.70(1)	4.3(3)	0.019(1)
Pt–Pt	5.56(1)	12	0.019(1)									Pt–Ru	4.33(1)	2.1(2)	0.019(3)
R-factor = 33				R-factor = 33				R-factor = 32				R-factor = 29			

ruthenium species assist platinum deposition. This may result in a layered deposition, followed by the reductive decomposition at 623 K. Temperature programmed reduction profiles of PtRu/CNT623 (SI 6) show a sharp H_2 consumption peak at 369 K attributed to ruthenium reduction, and a broad consumption region centered at 793 K that could be attributed to the gasification of surface carbon atoms of the support located at the vicinity of the PtRu particles [44]. Considering the fact that, contrary to samples PtRu/CNT973–1273, the sample PtRu/CNT623 presents a clear tendency towards the oxidation of Ru atoms (TPR, WAXS, XANES and EXAFS data), the ruthenium atoms should present a very different arrangement in this latter catalyst. The presence of surface oxygenated groups on the CNT surface may also contribute to ruthenium oxidation.

As mentioned in the previous section, the higher selectivity towards COL obtained with the PtRu/CNT973–1273 may result on the one hand from the larger particle size and on the other hand from a structural effect. The Ru enrichment of the nanoparticle should enhance the selectivity of the catalyst, and this promoting role of Ru can be explained via two mechanisms. (i) the Ru can act as an electropositive metal that increases the electron density on the Pt, thus decreasing the binding energies, particularly that of the C=C bond (inhibiting the adsorption via the C=C), and favors the hydrogenation of the C=O with respect to the C=C bond. This effect has been studied in detail by Delbecq and Sautet [45,46] by theoretical calculations. (ii) The electropositive Ru atoms, on the surface of Pt, act as electrophilic or Lewis acid sites for the adsorption and activation of the C=O bond via the lone electron pair of the oxygen atoms. This second mechanism, referred to as the "electrophilic C=O activation", was the most frequently invoked to account for the promoting effect of electropositive species [47,48]. Thus, since it is the presence of Ru surface atoms that should permit to increase the selectivity towards COL, a significant part of the ruthenium in sample PtRu/CNT623 could be present as an easily oxidized raft-like structure, not in association with Pt (strong Ru–O contribution in EXAFS), resulting from the high reactivity of the [Ru(COD)(COT)] precursor.

To support this hypothesis, the mobility of Pt and Ru adatoms on the CNT surface has been studied by means of DFT calculations in order to understand its impact on the nucleation of the nanoparticles. To obtain diffusion barriers associated with the hopping process of metallic atoms on the graphenic surface, it is mandatory to determine the lowest energy states, i.e. the most stable configurations (geometries) of the adsorbed species. With complete geometry relaxation of the planar graphenic model, it appears that in the case of Pt adatom, the most stable configuration is a bridging position above a C—C bond. This adsorption site is more stable by 0.2 eV (4.6 kcal/mol) over the hollow (in the middle of a hexagon) and on-top positions. Calculations performed on the small-diameter tube show that curvature's effect, on the one hand, tends to reduce energy differences between the different adsorption sites (on-top and bridge sites have almost the same energy) and, on the other hand, enhances globally the adsorption energy (by 0.4 eV), which results from a stronger binding. These results are in good agreement with previous studies [49,50]. The same general trends are obtained for Ru adatoms, with only one main difference: the hollow site is now more favored. The identification of the most stable sites done, we can estimate the diffusion barriers on the planar model more representative of the experimental conditions. In the case of Pt adatom, with a minimum energy path from one bridge to the nearest bridge position, the diffusion barrier is about 0.16 eV (3.7 kcal/mol). For the Ru adsorbed, the path is evidently from one hollow to the nearest hollow site, the diffusion barrier is now 0.65 eV. From those two estimates, it is clear that the hopping process controlling the diffusion of Pt or Ru adatoms is much easier in the case of Pt than Ru. In other words, Pt adatoms are more mobile than Ru ones.

Thus, we propose that the reductive decomposition of the grafted species at 623 K results in the formation of particles anchored on the support via a raft-like ruthenium rich base. At this point, well dispersed nanoparticles are produced on CNT support. A mean particle size of 2.7 nm has been measured from HRTEM, and a close one of 2.5 nm from WAXS. TEM and WAXS analyses show that these particles are small, strongly fcc, with a parameter pointing to the existence of a PtRu alloy. The strain of the lattice is measured isotropic and of around 4% from HRTEM diffractograms with respect to the pure Pt lattice, and of 1.5% from WAXS data. These crystalline particles contain between 40% (EDX spectra on single particles) and less than 50% (WAXS data) atomic fraction of Ru. Considering the theoretical atomic fraction of ruthenium (close to 66%) and the small contribution of the hcp character (WAXS), this is consistent with the existence at 623 K of a poorly ordered, easily oxidized ruthenium phase, as confirmed by EXAFS where the interference function at the Ru K-edge is characteristic of a very disordered structure with a significant contribution of the Ru–O bond in the first shell. Fig. 9 shows a representation of the sample PtRu/CNT623, which contains particles anchored on the support via a raft-like ruthenium rich base onto which alloyed platinum-rich particles are formed. These nanoparticles that should contain some PtRu alloy surface show higher selectivity towards the formation of COL (53%) than their monometallic counterparts (30–35%) [21].

The heat treatment under an inert atmosphere at 973 K of the sample PtRu/CNT623 does not affect significantly the mean particle size (2.9 nm from HRTEM and 3 nm from WAXS), pointing to the high stability of this catalyst, presumably due to the poor mobility of Ru on the CNT surface. Thus, the significant increase in selectivity towards COL should be correlated to a modification of the structure of the nanoparticles. From HRTEM, most of the particles of sample PtRu/CNT973 show an fcc structure with a non-isotropic compressive strain, around −9% along the (0 2 2) direction and −5% along the (2 0 0) one. These crystalline particles contain a higher amount of Ru atoms as determined from the fits of the EDX spectra (56% Ru at.%). From WAXS data, both fcc and hcp characters are observed. EXAFS and XANES clearly show that the heat treatment at 973 K induces the formation of an alloy with a

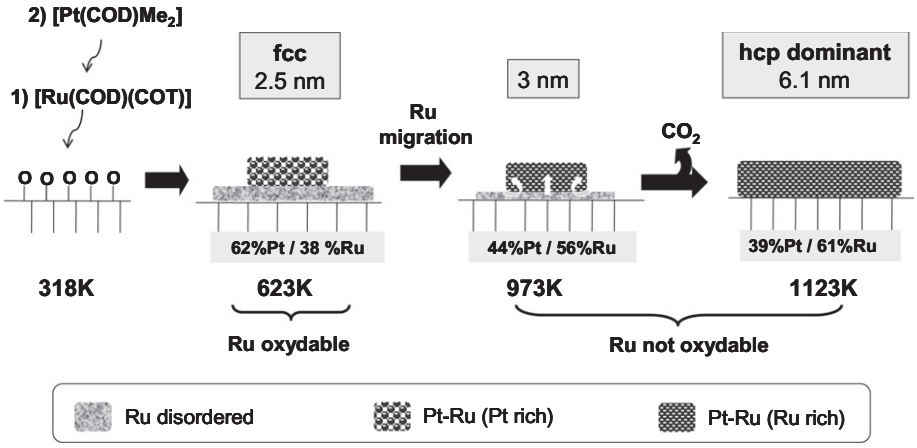

Fig. 9. Schematic representation of the evolution of the PtRu/CNT catalyst.

significant increase in Pt–Ru interactions. The results also indicate that the structural evolution of the Ru environment with the temperature of the thermal treatment is slower than that of the Pt environment, since the Ru environment of PtRu/CNT623 is significantly different from that of PtRu/CNT973 while the Pt environment is quite similar in PtRu/CNT623 and PtRu/CNT973. Thus, the higher number of Pt–Ru contacts on the alloy overlayer of the PtRu/CNT973 sample should be at the origin of the higher selectivity towards COL displayed by this catalyst. This structural modification does not alter the activity of the catalyst.

HRTEM and WAXS show that a further increase in the activation temperature at 1123 and 1273 K amplifies the phenomenon of structural ordering of the nanoparticles. Thus, from HRTEM sample, PtRu/CNT1123 shows a situation further evolved with respect to PtRu/CNT973: an fcc lattice with non-isotropic compressive strain of around −9% along the (2 0 0) lattice and of −8% in average on the two (1 1 1) axis. The final consideration being that the particles mainly tend to retain the original fcc structure of the platinum, with a compressive strain that increases with the treatment temperature, i.e. with the amount of Ru atoms in the lattice. Considering now the nanoparticle size, a clear increase in their mean diameter is noticed in this temperature range. This sintering can be correlated to the loss of the oxygen surface groups acting as anchoring sites for the nanoparticles, in this temperature range as shown from TPD profiles (SI 7) performed on PtRu/CNT623. In particular at 1273 K, the surface is almost free of oxygenated groups. The metal loading increases also as a function of the temperature of activation, indicating a loss of carbon during the heat treatment. Thus, for catalysts PtRu/CNT1123 and PtRu/CNT1273, both the ordering of the nanoparticles with an enrichment of the alloy in ruthenium and the increase of the nanoparticle size will contribute to the increase in the selectivity. Interestingly, whereas the mean particle size is significantly higher for these two latter catalysts than for the former ones, their catalytic activity is significantly higher. We believe that the greater conversion rates obtained after thermal treatment may be due to an effect of CNT surface chemistry on CAL adsorption or COL desorption that impacts the catalytic activity. The role of carbon material surface chemistry on the adsorption of different aromatic compounds has been discussed previously [51,52], and we propose that on heat-treated CNT samples, a π–π interaction between the CAL π electron ring and the basic π sites of the CNT surface may increase the CAL adsorption capacity, the CNT surface thus acting as reservoir of substrate where a high local concentration of CAL is readily accessible for the catalyst. Noteworthy and in the case of Pt on carbon nanofibers catalysts, it has been already suggested that hydrogenation is assisted by the adsorption of cinnamaldehyde on the carbon support after removal of the oxygen-containing surface groups [53]. Additionally, the removal of oxygenated groups might decrease the activation barrier for diffusion of CAL or COL on the CNT surface due to the absence of hydrogen bonds between the support and the substrate.

Acknowledgements

Dr. Fernando Pereira (Porto, Portugal) and Prof. Alain Kiennemann (Strasbourg, France) are greatly acknowledged for the TPD and TPR measurements, respectively. I. Gerber thanks the CALcul en MIdi-Pyrénées (CALMIP-p0812 project) for generous allocations of computer time. Part of this work was also performed using HPC resources from GENCI-[CINES] (Grant 2010-6005).

Appendix A. Supplementary material

Supplementary data associated with this article can be found, in the online version, at doi:10.1016/j.jcat.2010.11.016.

References

[1] T. Bligaard, Angew. Chem. Int. Ed. 48 (2009) 9782.
[2] R. Schlögl, S.B. Abd Hamid, Angew. Chem. Int. Ed. 43 (2004) 1628.
[3] A. Zecchina, E. Groppo, S. Bordiga, Chem. Eur. J. 13 (2007) 2440.
[4] J. Meurig Thomas, B.F.G. Johnson, R. Raja, G. Sankar, P.A. Midgley, Acc. Chem. Res. 36 (2003) 20.
[5] X. Pan, Z. Fan, W. Chen, Y. Ding, H. Luo, X. Bao, Nat. Mater. 6 (2007) 507.
[6] M.A. Mahmoud, C.E. Tabor, M.A. El-Sayed, Y. Ding, Z.L. Wang, J. Am. Chem. Soc. 130 (2008) 4590.
[7] S.C. Tsang, N. Cailuo, W. Oduro, A.T.S. Kong, L. Clifton, K.M. Kerry Yu, B. Thiebaud, J. Cookson, P. Bishop, ACS Nano 2 (2008) 2547.
[8] Y. Zhu, H. Qian, B.A. Drake, R. Jin, Angew. Chem. Int. Ed. 49 (2010) 1295.
[9] H. Falsig, B. Hvolbœk, I.S. Kristensen, T. Jiang, T. Bligaard, C.H. Christensen, J.K. Nørskov, Angew. Chem. Int. Ed. 47 (2008) 4835.
[10] W.F. Tuley, R.J. Adams, J. Am. Chem. Soc. 45 (1925) 3061.
[11] P. Gallezot, D. Richard, Catal. Rev. Sci. Eng. 40 (1998) 81.
[12] P. Maki-Arvela, J. Hajek, T. Salmi, D.Y. Murzin, Appl. Catal. A 292 (2005) 1.
[13] V. Ponec, Appl. Catal. A 149 (1997) 27.
[14] P. Claus, Top. Catal. 5 (1998) 51.
[15] J.M. Grosselin, C. Mercier, G.F. Allmang, Grass Organometall. 10 (1991) 2126.
[16] P. Serp, in: P. Serp, J.L. Figueiredo (Eds.), Carbon Materials for Catalysis, J. Wiley & Sons, Hoboken, NJ, 2009, p. 309.
[17] A. Jung, A. Jess, T. Schubert, W. Schütz, Appl. Catal. A 362 (2009) 95.
[18] Z. Guo, Y. Chen, L. Li, X. Wang, G.L. Haller, Y. Yang, J. Catal. (2010), doi:10.1016/j.jcat.2010.09.021.
[19] A. Solhy, B.F. Machado, J. Beausoleil, Y. Kihn, F. Gonçalves, M.F.R. Pereira, J.M. Órfão, J.L. Figueiredo, J.L. Faria, P. Serp, Carbon 46 (2008) 1194.
[20] B.F. Machado, H.T. Gomes, P. Serp, P. Kalck, J.L. Faria, Chem. Cat. Chem. 2 (2010) 190.
[21] H. Vu, F. Gonçalves, R. Philippe, E. Lamouroux, M. Corrias, Y. Kihn, D. Plee, P. Kalck, P. Serp, J. Catal. 240 (2006) 18.
[22] E. Castillejos, P.J. Debouttière, L. Roiban, A. Solhy, V. Martinez, Y. Kihn, O. Ersen, K. Philippot, B. Chaudret, P. Serp, Angew. Chem. 48 (2009) 2529.

[23] A.J. Plomp, H. Vuori, A.O.I. Krause, K.P. de Jong, J.H. Bitter, Appl. Catal. A 351 (2008) 9.
[24] M. Corrias, B. Caussat, A. Ayral, J. Durand, Y. Kihn, P. Kalck, P. Serp, Chem. Eng. Sc. 58 (2003) 4475.
[25] A. Solhy, B.F. Machado, J. Beausoleil, Y. Kihn, F. Gonçalves, M.F.R. Pereira, J.J.M. Órfão, J.L. Figueiredo, J.L. Faria, P. Serp, Carbon 46 (2008) 1194.
[26] F. Wen, H. Bönnemann, Appl. Organomet. Chem. 19 (2005) 94.
[27] K.V. Klementiev, Appl. Phys. 34 (2001) 209.
[28] S. Tomic, B.G. Searle, A. Wander, N.M. Harrison, A.J. Dent, J.F.W. Mosselmans, J.E. Inglesfield, CCLRC Technical Report DL-TR-2005-001, ISSN 1362-0207, CCRLC, Warrington, UK, 2004.
[29] S.J. Gurman, N. Binsted, I. Ross, J. Phys. C 17 (1984) 143.
[30] U. Von Barth, L. Hedin, J. Phys. C 5 (1972) 1629.
[31] E.D. Crozier, Nucl. Instr. Method Phys. Res. B 133 (1997) 134.
[32] Error Report of the International XAFS Society Standards and Criteria Committee, 2000, <http://ixs.iit.edu/subcommittee_reports/sc/>.
[33] A. Bianconi, in: D.C. Koninbsberger, R. Prins (Eds.), X-ray Absorption: Principles, Applications, Techniques of EXAFS, SEXAFS and XANES, Wiley, New York, 1988 (Chapter 11).
[34] G. Kresse, J. Furthmüller, Comput. Mater. Sci. 6 (1996) 15;
G. Kresse, J. Furthmüller, Phys. Rev. B 54 (1996) 11169.
[35] P.E. Blöchl, Phys. Rev. B 50 (1994) 17953;
G. Kresse, D. Joubert, Phys. Rev. B 59 (1999) 1758.
[36] J.P. Perdew, K. Burke, M. Ernzerhof, Phys. Rev. Lett. 77 (1996) 3865.
[37] P.E. Blöchl, O. Jepsen, O.K. Andersen, Phys. Rev. B 49 (1994) 16223.
[38] G. Henkelman, B.P. Uberuaga, H. Jonsson, J. Chem. Phys. 113 (2000) 9901;
G. Henkelman, H. Jonsson, J. Chem. Phys. 113 (2000) 9978.
[39] P. Serp, P. Kalck, R. Feurer, Chem. Rev. 102 (2002) 3085.
[40] C. Minot, P. Gallezot, J. Catal. 123 (1990) 341.
[41] E. Antolini, Mater. Chem. Phys. 78 (2003) 563.
[42] B.K. Teo, J. Am. Chem. Soc. 103 (1981) 3990.
[43] R.B. Greegor, F.W. Lytle, J. Catal. 63 (1980) 476.
[44] M. Cerro-Alarcón, A. Maroto-Valiente, I. Rodríguez-Ramos, A. Guerrero-Ruiz, Carbon 43 (2005) 2711.
[45] F. Delbecq, P. Sautet, J. Catal. 165 (1996) 152.
[46] R. Hirschl, F. Delbecq, P. Sautet, J. Hafner, J. Catal. 217 (2003) 354.
[47] J.P. Breen, R. Burch, J. Gomez-Lopez, K. Griffin, M. Hayes, Appl. Catal. A: Gen. 268 (2004) 267.
[48] D. Richard, J. Ockelford, A. Giroir-Fendler, P. Gallezot, Catal. Lett. 3 (1989) 53.
[49] G. Chen, Y. Kawazoe, Phys. Rev. B 73 (2006) 125410.
[50] H.C. Dam, N.T. Cuong, A. Sugiyama, T. Ozaki, A. Fujiwara, T. Mitani, S. Okada, Phys. Rev. B 79 (2009) 115426.
[51] T. Garcia, R. Murillo, D. Cazorla-Amoros, A.M. Mastral, A. Linares-Solano, Carbon 42 (2004) 1683.
[52] D.M. Nevskaia, E. Castillos-Lopez, A. Guerrero-Ruiz, V. Munoz, Carbon 42 (2004) 653.
[53] M.L. Toebes, Y. Zhang, J. Hájek, T.A. Nijhuis, J.H. Bitter, A.J. van Dillen, D.Y. Murzin, D.C. Koningsberger, K.P. de Jong, J. Catal. 226 (2004) 215.